Title

Cancer-stromal cell interactions in breast cancer brain metastases induce glycocalyx-mediated resistance to HER2-targeting therapies.

Permalink

https://escholarship.org/uc/item/08k4s6sx

Journal

Proceedings of the National Academy of Sciences, 121(20)

Authors

Goyette, Marie-Anne

Stevens, Laura

DePinho, Carolyn

et al.

Publication Date

2024-05-14

DOI

10.1073/pnas.2322688121

Peer reviewed

Cancer–stromal cell interactions in breast cancer brain metastases induce glycocalyx-mediated resistance to HER2-targeting therapies

Marie-Anne Goyette[a,b,c,1], Laura E. Stevens[a,b,c,1], Carolyn R. DePinho[a], Marco Seehawer[a,b,c], Jun Nishida[a,b,c], Zheqi Li[a,b,c], Callahan M. Wilde[a], Rong Li[d], Xintao Qiu[d], Alanna L. Pyke[a], Stephanie Zhao[a], Klothilda Lim[d], Gabrielle S. Tender[e], Jason J. Northey[f], Nicholas M. Riley[e], Henry W. Long[d], Carolyn R. Bertozzi[e,g,h] 🆔, Valerie M. Weaver[f,i,j,k,l,m] 🆔, and Kornelia Polyak[a,b,c,2] 🆔

Brain metastatic breast cancer is particularly lethal largely due to therapeutic resistance. Almost half of the patients with metastatic HER2-positive breast cancer develop brain metastases, representing a major clinical challenge. We previously described that cancer-associated fibroblasts are an important source of resistance in primary tumors. Here, we report that breast cancer brain metastasis stromal cell interactions in 3D cocultures induce therapeutic resistance to HER2-targeting agents, particularly to the small molecule inhibitor of HER2/EGFR neratinib. We investigated the underlying mechanisms using a synthetic Notch reporter system enabling the sorting of cancer cells that directly interact with stromal cells. We identified mucins and bulky glycoprotein synthesis as top-up-regulated genes and pathways by comparing the gene expression and chromatin profiles of stroma-contact and no-contact cancer cells before and after neratinib treatment. Glycoprotein gene signatures were also enriched in human brain metastases compared to primary tumors. We confirmed increased glycocalyx surrounding cocultures by immunofluorescence and showed that mucinase treatment increased sensitivity to neratinib by enabling a more efficient inhibition of EGFR/HER2 signaling in cancer cells. Overexpression of truncated MUC1 lacking the intracellular domain as a model of increased glycocalyx-induced resistance to neratinib both in cell culture and in experimental brain metastases in immunodeficient mice. Our results highlight the importance of glycoproteins as a resistance mechanism to HER2-targeting therapies in breast cancer brain metastases.

breast cancer | brain metastasis | HER2 | resistance | stroma

Distant metastasis is the major cause of cancer-associated mortality, with brain metastasis being particularly challenging to treat with few therapeutic options (1, 2). Patients with triple-negative (TNBC) and HER2-positive breast cancer are at particularly high risk of brain metastasis (3). 31 to 50% of patients with HER2-positive metastatic breast cancer develop brain metastasis, which frequently exhibits resistance to treatment, even when tumors in other parts of the body are under control (3–5). In patients treated with trastuzumab, a monoclonal antibody targeting HER2, the brain often becomes the initial and sole site of metastatic relapse (6). Resistance was thought to be due to the inability of certain agents like antibodies to cross the blood–brain barrier (BBB) and penetrate the brain parenchyma. However, multiple studies have revealed that the BBB is often compromised in brain metastatic patients; thus, ineffective drug penetration into the brain cannot fully explain therapeutic resistance (7).

The tumor microenvironment (TME) plays key roles in driving tumor progression and therapeutic resistance (8). The brain has a unique molecular and cellular environment and cancer cell–brain cell interactions have been identified as drivers of tumor growth and resistance to treatment (9–12). For example, microglia, a type of immune cell in the brain, become activated in the vicinity of metastases and can promote tumor growth (9). Neurons have also been identified as promoters of brain metastasis growth, and breast cancer cells can modulate neuronal signaling pathways to enhance their colonization (10). Additionally, direct interactions between lung or breast cancer cells and astrocytes provide support for tumor growth and resistance to chemotherapy by activating the STAT1 and NFκB pathways (11). In order to colonize the brain, tumor cells must cross the BBB, which is composed of endothelial cells, pericytes, vascular smooth muscle cells, and astrocytes. Following extravasation, tumor cells can co-opt the vasculature and alter endothelial and mural cell signaling, leading to changes in vascular leakiness and immune cell recruitment (13, 14). Consequently, heterogeneity due to spatial location and contact with various stromal cells can affect cancer cell fate during treatment.

Significance

The development of HER2-targeted therapies significantly improved the clinical outcomes of patients with HER2-positive breast cancer, but brain metastasis remains a major clinical challenge. Understanding the underlying mechanisms will facilitate the development of more effective therapeutic strategies. Here, we report that breast cancer brain metastasis stromal cells induce resistance to HER2-targeting agents via up-regulating bulky glycoproteins and that mucinase treatment can partially reverse stroma-induced resistance.

The glycocalyx is a meshwork of glycoproteins and glycolipids decorating the cell surface of cells including the mammary epithelium and influences cell interaction with the microenvironment (15). It is often thickened on cancer cells where it can promote cancer cell survival and metastasis (16–18). Mucins, a family of secreted or transmembrane glycoproteins characterized by dense regions of O-glycosylation, are an important component of the glycocalyx and have been implicated in therapy resistance by shielding the surface of cancer cells and by inducing the clustering of cell surface receptors mediating oncogenic signals (19–22).

Here, we investigated gene expression and chromatin changes induced by direct contact between brain metastasis stromal cell (BMSC) and HER2+ breast cancer cells, before and after treatment with neratinib, a small molecule inhibitor of HER2/EGFR. We also performed follow-up validation of top hits in cell culture and in vivo as well as in clinical patient samples. Our results suggest that targeting the glycocalyx could improve the efficacy of HER2-targeting agents in brain metastases of breast cancer.

Results

Metastatic Brain Stromal Cell Interactions Induce Resistance to HER2-targeted Therapies. To investigate interactions between HER2+ breast cancer cells and BMSCs, brain metastases from multiple cases (BMSC1, BMSC2, BMSC3, *SI Appendix*, Table S1) were dissociated and stromal cell primary cultures were initiated as previously described (23). We performed RNA-seq to analyze the cellular composition of the resulting cell cultures. Assessing cell type-specific markers from published brain metastasis single-cell RNA sequencing data (13) revealed that BMSC3 cells do not express canonical markers of astrocytes, macrophages, endothelial, neuronal, or cancer cells, but instead strongly express markers of mural cells including PDGFRβ and α-SMA (*SI Appendix*, Fig. S1A). To confirm this prediction and to assess the heterogeneity of our BMSC primary cultures, we performed immunostaining for the most common mural cell markers PDGFRβ and α-SMA in all three BMSC primary cultures and found that all cells are positive for PDGFRβ, and a small subset also expresses α-SMA (*SI Appendix*, Fig. S1B). Based on these data, we conclude that BMSCs grown in vitro resemble pericytes.

To study the interaction of these BMSCs with cancer cells, we developed a physiologically relevant coculture model where cells were grown in 5% Matrigel to form 3D organoids (Fig. 1A). A panel of HER2+ breast cancer cell lines (MDA-MB-453, HCC1954, BT-474, ZR-75-30, and 21NT) was engineered to express mCherry and luciferase to enable cancer cell-specific viability measurements. Cancer cells growing in 3D organoids alone or mixed with BMSCs were treated with increasing doses of various HER2-targeted therapies, including small molecule inhibitors of HER2-family kinases (lapatinib, tucatinib, and neratinib), the antibody-drug conjugate trastuzumab deruxtecan (T-DXd), and with chemotherapy (5-fluoro-uracil, 5-FU). Differences in response between cancer cell mono- and cocultures were determined by calculating the differences in the areas under the curve (AUC) of the dose–response experiment. Cancer cells were more resistant to treatment to most agents when cocultured with BMSCs, with neratinib showing the strongest resistance and consistent differences across cell lines (Fig. 1 B and C). Therefore, we investigated the mechanism of BMSC-mediated resistance to neratinib in further detail.

Establishment of a BMSC-contact Reporter System using SynNotch. Spatial heterogeneity within tumors due to variable stromal niches could impact tumor cell epigenetic and transcriptomic profiles increasing intratumor cellular heterogeneity and enabling the development of resistant subclones (24). To investigate direct BMSC contact–induced molecular and phenotypic changes, we designed a reporter system using the Synthetic Notch (SynNotch) approach to identify tumor cells that have come in direct contact with stroma (25). We engineered mCherry⁺ breast cancer cells to express SynNotch, which contains an extracellular anti-GFP nanobody, and BMSCs to express cell surface GFP. Upon direct cell–cell interaction, the intracellular domain is released, leading to the induction of BFP (*SI Appendix*, Fig. S2A and Fig. 1D). We used SynNotch-MCF10DCIS cells cultured in 3D to test the functionality of the system and confirmed the induction of BFP expression in cells in contact with GFP⁺ BMSC3 (*SI Appendix*, Fig. S2B). When cultured at a 1:1 ratio of SynNotch-MCF10DCIS cells to GFP⁺ BMSCs, 59.1% of mCherry⁺ cells became BFP⁺ as detected by flow cytometry (*SI Appendix*, Fig. S2C). To determine the stability of BFP induction following contact with stroma, SynNotch-MCF10DCIS cells were sorted into mCherry⁺BFP⁻ and mCherry⁺BFP⁺ populations following 3D culture with GFP⁺BMSC3s. The expression of BFP was then assessed 6, 24, 48, and 72 h postcontact with GFP⁺BMSC3s. BFP expression gradually declined after 24 h but remained above baseline even at 72 h (*SI Appendix*, Fig. S2D). Finally, to determine the ratio of BMSCs that would allow for a heterogeneous cell population containing both contact and no-contact cancer cells, we performed live cell imaging for 48 h at increasing ratios of cancer cells to BMSCs. We found that BMSCs were very motile and when cultured at a 1:1 ratio, almost all cancer cells have come in contact with BMSCs (*SI Appendix*, Fig. S2E and Movie S1). Using both live cell imaging and fluorescence activated cell sorting (FACS), we determined that higher ratios of cancer cells (10:1, 5:1, and 3:1) to BMSCs were ideal to maintain both contact and no-contact populations in the same coculture (*SI Appendix*, Fig. S2 E and F). We then engineered SynNotch-MDA-MB-453 and SynNotch-HCC1954 cells to investigate the effect of BMSC contact on resistance to neratinib.

Transcriptomic and Chromatin Changes Induced in Cancer Cells by BMSC Contact. To identify BMSC contact–induced gene expression changes, we cocultured cancer cells with GFP⁺BMSC3 at a high cancer to stromal cell ratio (MDA-MB-453 10:1 and HCC1954 3:1) to ensure the presence of both contact and no-contact cells (Fig. 1D). Following 24 h of growth in 3D to allow organoids to form, cultures were treated with vehicle (DMSO) or neratinib for 48 h. Organoids were then dissociated and mCherry⁺BFP⁻ (breast cancer cell, no-contact) and mCherry⁺BFP⁺ (breast cancer cell, stroma-contact) cells were purified by FACS, and profiled using RNA-seq (Fig. 1 D and E and *SI Appendix*, Fig. S2G).

We investigated gene expression alterations induced by BMSC contact and neratinib by comparing cells in monoculture (mCherry⁺ in monoculture) and coculture (mCherry⁺BFP⁺ in coculture) with or without neratinib treatment. We then compared DMSO or neratinib-treated cells in mono- and coculture (BMSC contact–induced genes) and cells growing in mono- or coculture treated with DMSO or neratinib (neratinib-induced genes) (Datasets S1 and S2). Overall, neratinib had a lesser impact on gene expression in coculture than in monoculture as there were significantly fewer differentially expressed genes (DEGs) (Fig. 2A). BMSC contact increased the expression of genes with known roles in G2/M phase of the cell cycle (e.g., AURKA, BUB1) in MDA-MB-453 cells implying increased proliferation or G2/M arrest, and this was apparent in both DMSO and neratinib-treated cells and may contribute to treatment resistance (Datasets S1). In contrast, in HCC1954 cells, top contact-induced genes were related to
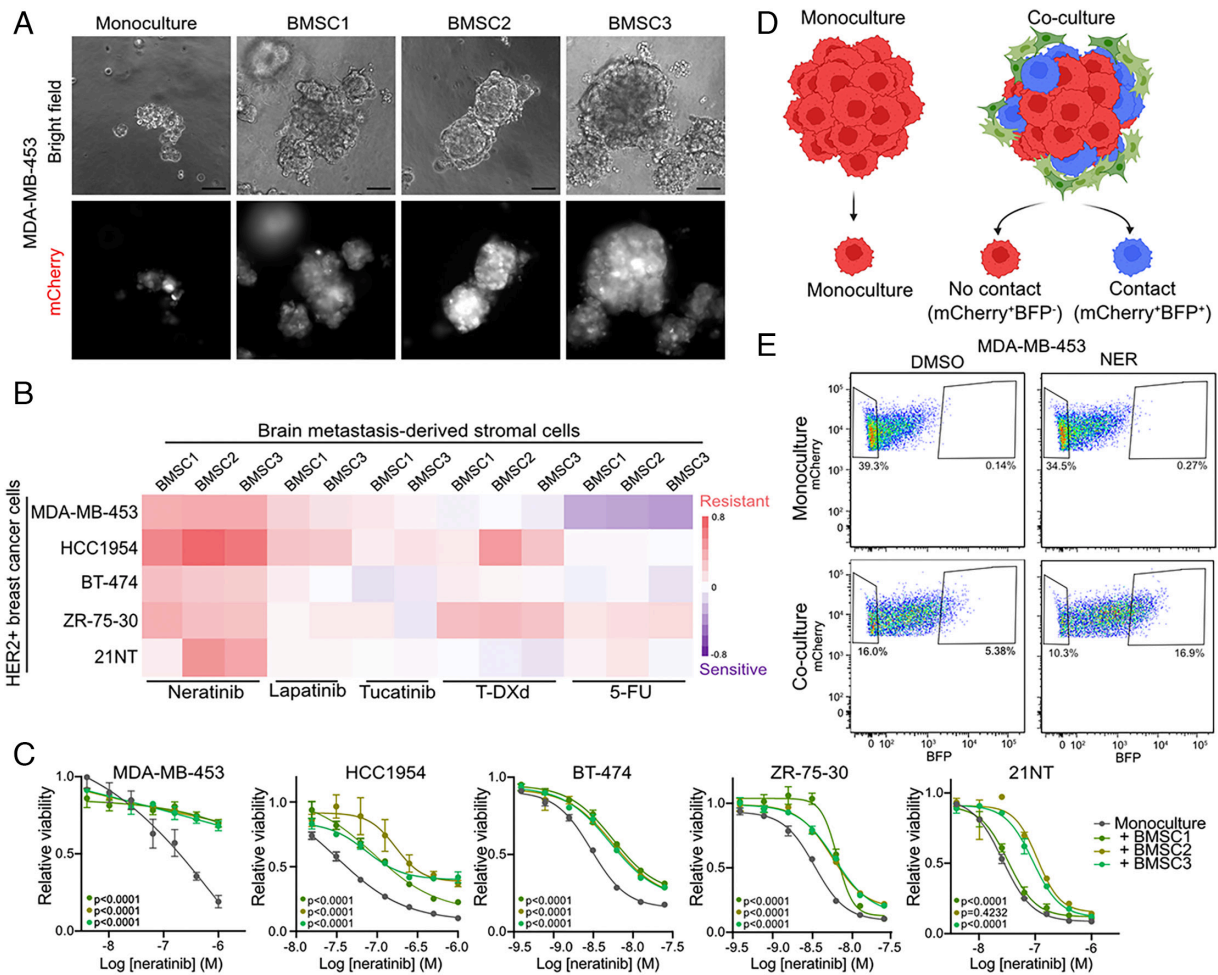
Fig. 1. 3D cultures of HER2+ breast cancer and brain metastasis stromal cells. (*A*) Representative images of MDA-MB-453 cells cultured in 5% matrigel in 3D in monoculture or cocultured with indicated BMSCs for 5 d. (Scale bar, 100 μm.) (*B*) Heatmap showing the effect of coculture with BMSC on the viability of HER2+ breast cancer cells following treatment with the indicated treatments. Protection (pink) or sensitization (purple) to treatment is calculated by the difference between the AUC of monoculture vs. coculture with different brain stroma cells [(AUC$_{monoculture}$ − AUC$_{coculture}$)/AUC$_{monoculture}$]. (*C*) Relative cell viability of the HER2+ breast cancer cells treated with increasing doses of neratinib in monoculture or in coculture with BMSCs (two-way ANOVA, mean, and SEM). (*D*) Schematic representation of the SynNotch reporter model (created with BioRender.com). (*E*) Representative flow cytometry plots depicting gating strategy. BMSCs were excluded by gating out GFP⁺ cells. No-contact cancer cells were sorted by gating for GFP⁻mCherry⁺BFP⁻ cells, while BMSC contact cancer cells were GFP⁻mCherry⁺BFP⁺.

immunity (e.g., HLA-DQA1) and mesenchymal cell state (e.g., VIM, TNC) (Datasets S1). Gene set enrichment analysis (GSEA) (26, 27) on genes differentially expressed between DMSO control and neratinib in mono- and coculture showed substantial overlap in down-regulated signatures between the two cell lines, while up-regulated pathways were distinct (Fig. 2 *B* and *C* and *SI Appendix,* Fig. S3 *A* and *B*). Metabolism-related pathways including MTORC1 signaling, hypoxia, glycolysis, and cholesterol homeostasis were decreased by neratinib treatment regardless of culture conditions in both MDA-MB-453 and HCC1954 cells. HCC1954 cells also showed a strong decrease of cell cycle-related signatures such as E2F and MYC targets and G2M checkpoint suggesting cell cycle arrest (Fig. 2*C* and *SI Appendix,* Fig. S3 *B* and *C*). In MDA-MB-453 cells, coculture increased the metabolic pathways that were down-regulated by neratinib (Fig. 2*D*). Coculture also increased epithelial-to-mesenchymal transition (EMT) signature in both cell lines (Fig. 2 *D* and *E* and *SI Appendix,* Fig. S3 *C* and *D*).

Next, we explored the predicted transcriptional regulators of genes induced in coculture in both DMSO and neratinib-treated conditions using Landscape In Silico deletion Analysis (LISA) algorithm (28). We found multiple overlapping hits between the two cell lines including NR3C1 (glucocorticoid receptor), AR (androgen receptor), ESR1 (estrogen receptor), and FOXA1 (Fig. 2*F*) implying that they may act as potential regulators of

coculture-induced changes. Several of these transcription factors are known regulators of luminal cell differentiation (e.g., FOXA1), while NR3C1 may be linked to the observed metabolic changes. Shift in cell state can be controlled through epigenetic mechanisms and this has previously been associated with therapeutic resistance (24). Thus, since even short-term BMSC contactinduced resistance-associated transcriptional programs in breast cancer cells, we further explored whether these changes may be mediated by epigenetic mechanisms.

While prior studies have described distinct epigenetic profiles of cancer-associated fibroblasts and other stromal cell types within the TME (29–31), the impact of direct stromal cell contact on cancer cell chromatin profiles remains unexplored. Therefore, we aimed to investigate the influence of stromal cell contact on tumor cell chromatin accessibility using assay for transposase-accessible chromatin with sequencing (ATAC-seq). Because our reporter system is transient and can only reliably detect contact in a 72 h time period and epigenetic changes may need more time to become evident, we could not reliably isolate contact and no-contact cells from the same coculture as done for the RNA-seq experiment. Thus, we grew mCherry⁺ cancer cells in monoculture or in coculture at a 1:2 ratio of BMSCs to ensure that most cancer cells came in contact with BMSCs. Cells were treated with DMSO or neratinib for 7 d, mCherry⁺ cancer
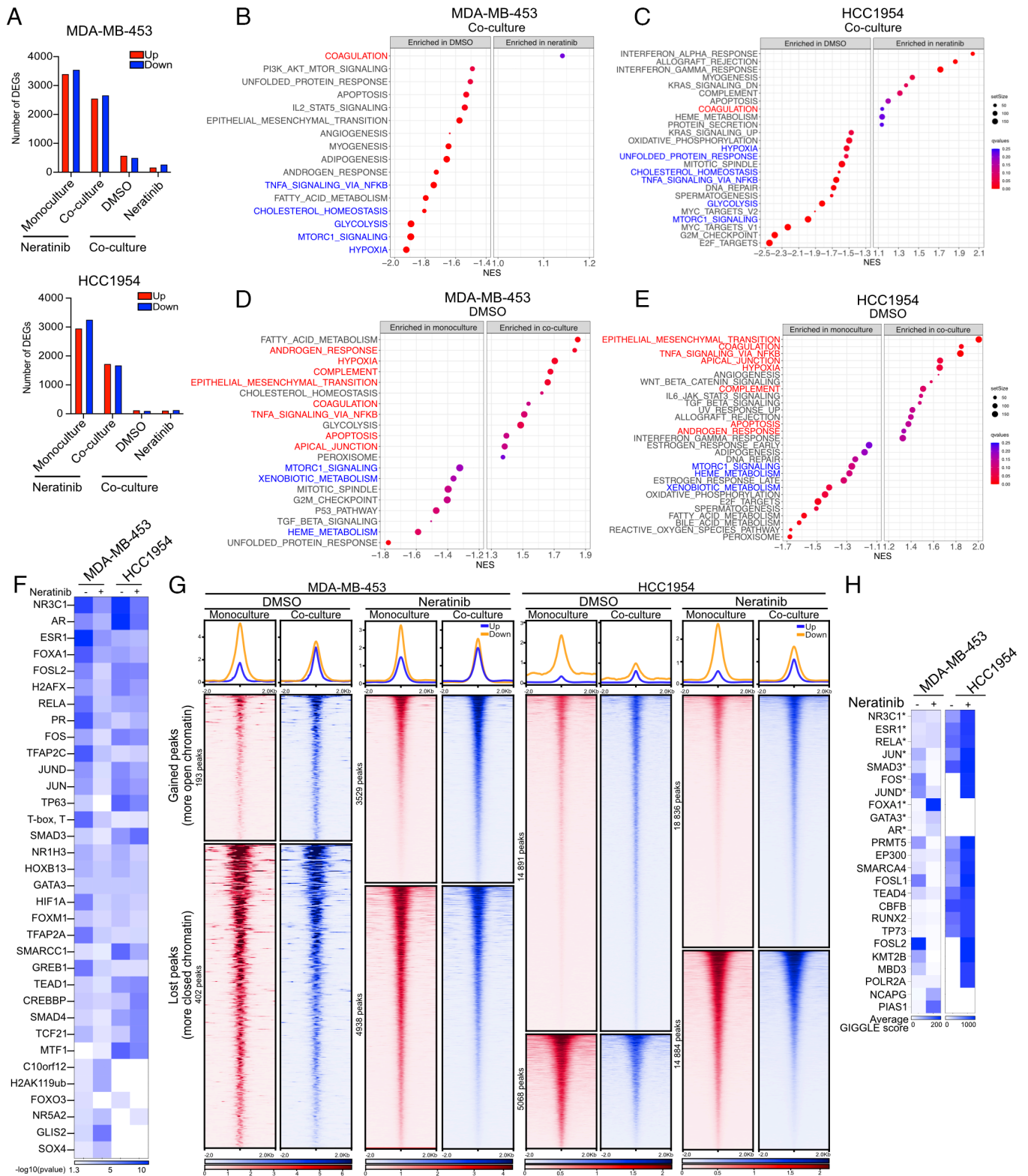
Fig. 2. Transcriptomic and chromatin changes in cancer cells induced by interaction with BMSCs in the presence or absence of neratinib. (*A*) Bar graph showing the number of DEGs comparing monoculture and coculture (mCherry⁺BFP⁺ contact cells) upon DMSO or neratinib treatment. (*B* and *C*) GSEA of MDA-MB-453 or HCC1954 cell RNA-seq data in coculture comparing DMSO and neratinib treatment. (*D* and *E*) GSEA of MDA-MB-453 and HCC1954 RNA-seq data in the DMSO condition comparing monoculture and contact cells in coculture (red and blue pathway labels indicate shared up- or down-regulated pathways, respectively). (*F*) Heatmap of predicted transcription regulators from LISA algorithm of up-regulated genes in coculture. Top 10 most significant hits of each condition are included. (*G*) Representative heatmap showing significantly gained or lost peaks in cancer cells in monoculture (red) or coculture (blue) with or without neratinib treatment. Summary plots indicating intensities for all gained (blue) or lost (orange) peaks are shown at the top (n = 2 biological replicates per group). (*H*) Heatmap of GIGGLE analysis showing top 10 hits up in coculture. (* means overlap with LISA from Panel *F*).

cells were then isolated by FACS and profiled using ATAC-seq (Datasets S3 and S4).

Analysis of ATAC-seq data revealed a number of differential peaks between monoculture and coculture in DMSO and neratinib in both cell lines (Fig. 2G and Datasets S3 and S4), demonstrating that stromal contact can change chromatin accessibility. Evaluation of the genomic location of the differential ATAC-seq peaks revealed that in MDA-MB-453 cells cocultured with BMSC, more peaks were gained in promoter regions in neratinib-treated cells compared to DMSO control, which gained more peaks localized at distant intergenic regions (SI Appendix, Fig. S3E). In HCC1954 cells, coculture also changed chromatin openness in nonpromoter regions in both DMSO and neratinib-treated conditions (SI Appendix, Fig. S3E). By integrating RNA-seq and ATAC-seq datasets, in HCC1954 cells, we found that up-regulated genes associated with gained ATAC-seq peaks were enriched for EMT signature genes including PMEPA1, TNC, ITGB3, TGFBI, and SERPINE1 (SI Appendix, Fig. S3F). MMP13 was also strongly up-regulated, and its locus had more open chromatin in the coculture independently of neratinib treatment (SI Appendix, Fig. S3 F and G). GIGGLE analysis correlating known binding motifs to the ATAC-seq dataset identified multiple transcription factors that overlapped with the LISA analysis of the RNA-seq data, including the top hits NR3C1, ESR1, FOXA1, and AR (Fig. 2H), suggesting their importance in driving the BMSC coculture-induced epigenetic and transcriptomic changes. These data suggest that BMSC contact–induced therapeutic resistance may in part be driven by changes in chromatin patterns, which implies that even short-term stromal contact may induce hereditary treatment resistance in cancer cells.

Direct BMSC Contact Up-regulates Glycoproteins in Breast Cancer Cells. Next, we compared the gene expression profiles of contact and no-contact cancer cells from the same coculture to investigate cellular heterogeneity due to direct BMSC interaction. In the HCC1954 model, we did not detect any significant DEGs between contact and no-contact cells possibly due to the higher cancer-to-stromal cell ratio used (3:1 vs. 10:1 in MDA-MB-453 cells) likely causing all cancer cells to be in contact with BMSCs. In contrast, in the MDA-MB-453 model, we identified 65 and 39 genes with significantly higher and lower expression in BMSC-contact compared to no-contact cancer cells from the same coculture (Fig. 3A and Dataset S5). LISA of DEGs predicted RARA, CARM1, HIVEP1, AGO1, and IGF1R as regulators of contact cell-specific transcriptional changes with IGF1R being only observed in DMSO-treated cells (SI Appendix, Fig. S4A).

MUC2 and MUC5B were among the top BMSC contact–induced genes with MUC2 showing more than 15-fold increase in expression (Fig. 3A). Mucins are large transmembrane or secreted glycoproteins expressed in epithelial cells contributing to the formation of the glycocalyx (20). Increased glycocalyx and mucins have been shown to play a role in treatment resistance and metastasis (16, 17, 21, 22, 33); thus, the upregulation of MUC2 and MUC5B by BMSC contact may contribute to the observed stroma-contact-induced neratinib resistance in BMSC cocultures. Pathway enrichment analysis with genes located nearest to gained ATAC-seq peaks in coculture in nonpromoter regions also showed enrichment for O-linked glycosylation of mucins and ECM proteoglycans in MDA-MB-453 and HCC1954 cells, respectively, suggesting that BMSC contact–induced upregulation of protein glycosylation may be mediated by epigenetic mechanisms (SI Appendix, Fig. S4 B and C).

To further explore BMSC contact–induced protein glycosylation changes, we performed a GSVA on the RNA-seq data derived from

contact and no-contact cells. Many glycosylation-related signatures including bulky glycoproteins, glycosylation, and glycoprotein biosynthesis, showed enrichment in BMSC contact MDA-MB-453 cancer cells and some of these signatures were further enriched by neratinib treatment (Fig. 3B). Scores for glycosyltransferases were enriched by neratinib treatment regardless of culture conditions, while the ECM glycoproteins signature was generally increased in the coculture in both MDA-MB-453 and HCC1954 cells (Fig. 3B and SI Appendix, Fig. S4D). HCC1954 did not show an increase of mucins in coculture potentially due to high baseline levels compared to MDA-MB-453 cells (SI Appendix, Fig. S4 D and E). To validate our findings in clinical samples, RNA-seq data from primary breast cancer and matched brain metastasis (32) were queried with glycosylation signatures. An enrichment of the ECM glycosylation signature was found in brain metastases independent of breast tumor subtype (Fig. 3C) with a similar trend seen in the HER2-positive subset (SI Appendix, Fig. S4F). Likewise, glycoprotein biosynthesis showed a trend toward enrichment in brain metastasis (SI Appendix, Fig. S4G). Thus, an increase of glycoproteins like mucins may be a potential resistance mechanism induced by stromal cells in breast cancer brain metastases.

BMSC Contact–induced Mucin Glycoproteins Make HER2+ Cancer Cells Resistant to Neratinib. To confirm the increase in mucin expression in BMSC cocultures and their possible role in neratinib resistance, we used the mucin-selective protease of C1 esterase inhibitor (StcE) to proteolyze mucins and an inactive form of StcE (StcE^{E447D}) to visualize mucins (34). The StcE mucinase is selective for a distinct peptide- and glycan-based motif enabling specific binding and cleavage of mucins (34–36). First, we used biotin-StcE^{E447D} to stain for mucin glycoproteins in 3D cocultures of GFP$^+$ BMSCs and H2B-mCherry$^+$ HER2+ cell lines MDA-MB-453, HCC1954, and BT-474. We detected enrichment of mucins surrounding the organoids in BMSC cocultures compared to monocultures, confirming our RNA-seq data (Fig. 3 D and E). To determine whether this upregulation of mucins affects the physical interaction of BMSCs with cancer cells, we treated the SynNotch reporter organoids with StcE. Mucinase treatment increased the number of stromal-contact cancer cells from ~15 to ~22% suggesting a relatively mild effect of mucins on the direct interaction between BMSC and cancer cells in these 3D organoid cultures (SI Appendix, Fig. S5 A–C).

Next, we investigated the effect of mucinase treatment on therapeutic responses. We found that mucinase treatment did not impact the sensitivity of cancer cells to neratinib in monocultures, but significantly increased sensitivity in BMSC cocultures (Fig. 3F). In addition, BMSC coculture reduced the inhibitory effect of neratinib on phospho-EGFR and downstream signaling components, which was reversed by the addition of StcE, demonstrating a direct link between BMSC contact, mucins, and neratinib resistance (Fig. 3G). Mucinase treatment also improved sensitivity to other HER2-targeting agents such as tucatinib and T-DXd in MDA-MB-453 and BT-474 but not in HCC1954 cells, and it did not affect response to 5-FU chemotherapy in any of the cell lines tested (SI Appendix, Fig. S5D).

To determine whether the BMSC-induced upregulation of mucins is dependent on direct BMSC-cancer cell contact, we tested the effects of BMSC-conditioned media on cancer cell monocultures in the presence and absence of neratinib treatment. BMSC-conditioned media did not consistently affect neratinib sensitivity across cell lines (SI Appendix, Fig. S5E). In line with this, expression of mucins was not affected by BMSC-conditioned media in cancer cell monocultures, suggesting that BMSC-
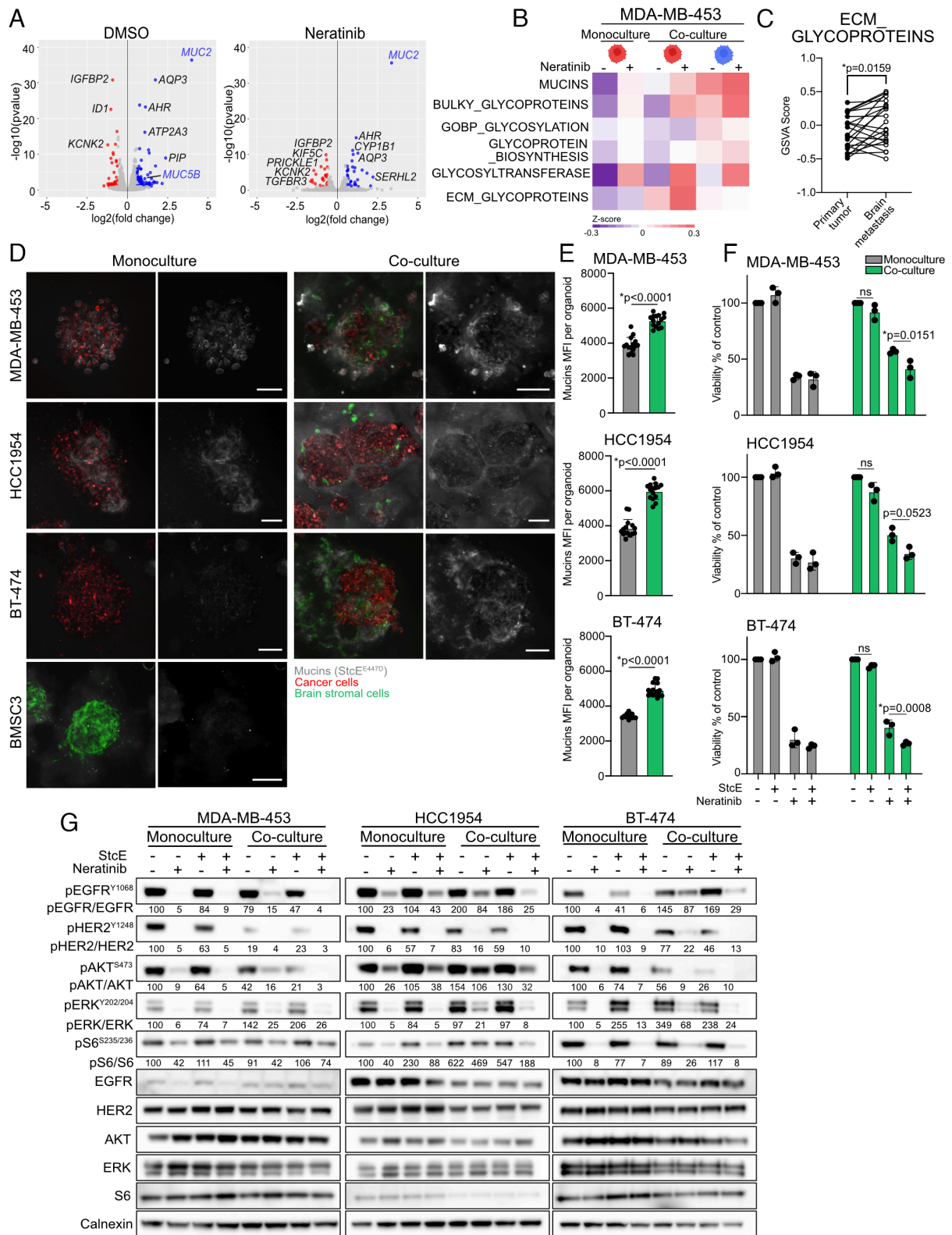
Fig. 3. Direct contact with BMSC causes elevated mucin glycoprotein levels on organoids leading to increased resistance to neratinib. (*A*) Volcano plot of genes differentially expressed in MDA-MB-453 cells in direct contact with BMSC compared to no-contact cells in the same coculture. *MUC2* and *MUC5B* are highlighted in blue. (*B*) Heatmap of Gene Set Variation Analysis (GSVA) for glycosylation signatures. (*C*) GSVA of ECM glycoprotein refined signature on RNA-seq of matched primary tumor and brain metastasis from ref. 32 (Wilcoxon test). (*D*) Representative images of immunofluorescence for mucins (StcE^{E447D}, gray) in 3D organoids formed by cancer cells (H2B-mCherry+, red) and BMSC3s (GFP+, green). (Scale bar, 100 μm.) (*E*) Quantification of mucin signal from Panel D by measuring mean fluorescence intensity (MFI) for 15 organoids, (n = 3 independent experiments with five organoids per experiment, Student's *t*-test, mean, and SD). (*F*) Treatment with StcE mucinase (10 nM) increases the sensitivity of cancer cells to 500 nM neratinib in BMSC cocultures (n = 3 independent experiments, one-way ANOVA with multiple comparisons, mean and SD). (*G*) Immunoblot analysis of EGFR/HER2 signaling pathway components in cancer cells from 3D monoculture or BMSC cocultures in the presence or absence of 50 nM neratinib with and without a 1 h incubation with 10 nM StcE.

induced resistance due to mucin requires direct contact (*SI Appendix,* Fig. S5 *F* and *G*).

Overall, these data support the hypothesis that the upregulation of mucins in cancer cells is induced by direct contact with BMSC and that this is mediating resistance to HER2-targeting therapies.

A Bulky Glycocalyx Decreases Sensitivity to Neratinib. To examine whether increase of the bulky glycocalyx in HER2+ breast cancer cells would lead to neratinib resistance, we overexpressed MUC1ΔCT, a truncated form of MUC1 lacking its cytoplasmic tail (33), under the control of a doxycycline (dox)-inducible promoter in HCC1954, MDA-MB-453, and BT-474 HER2+ breast cancer cell lines (Fig. 4*A*). In 3D culture, MUC1ΔCT-expressing cancer cells formed smaller cell clusters with more cells remaining as single cells compared to empty vector (EV), which is in line with an increase

in glycocalyx diminishing cell–cell contact (*SI Appendix,* Fig. S6A). MUC1ΔCT-expressing HER2+ breast cancer cells were also more resistant to neratinib (Fig. 4*B*) as well as to other HER2-targeting agents T-DXd and tucatinib (*SI Appendix,* Fig. S6B). MUC1ΔCT overexpression also diminished the inhibitory effects of neratinib on EGFR/HER2 signaling, mimicking our observations in BMSC cocultures (Fig. 4*C*). Furthermore, in this model, the increase of glycocalyx bulk reduced EGFR and HER2 total protein levels, but the ratio of pEGFR/EGFR and pHER2/HER2 was increased at the baseline level.

To validate our findings in vivo, MDA-MB-453 cells expressing H2B-mCherry-Luciferase2 and EV or MUC1ΔCT were injected intracardially into NSG mice to induce experimental brain metastases. The expression of EV or MUC1ΔCT was induced by feeding mice with doxycycline-containing diet three days after cancer cell injection
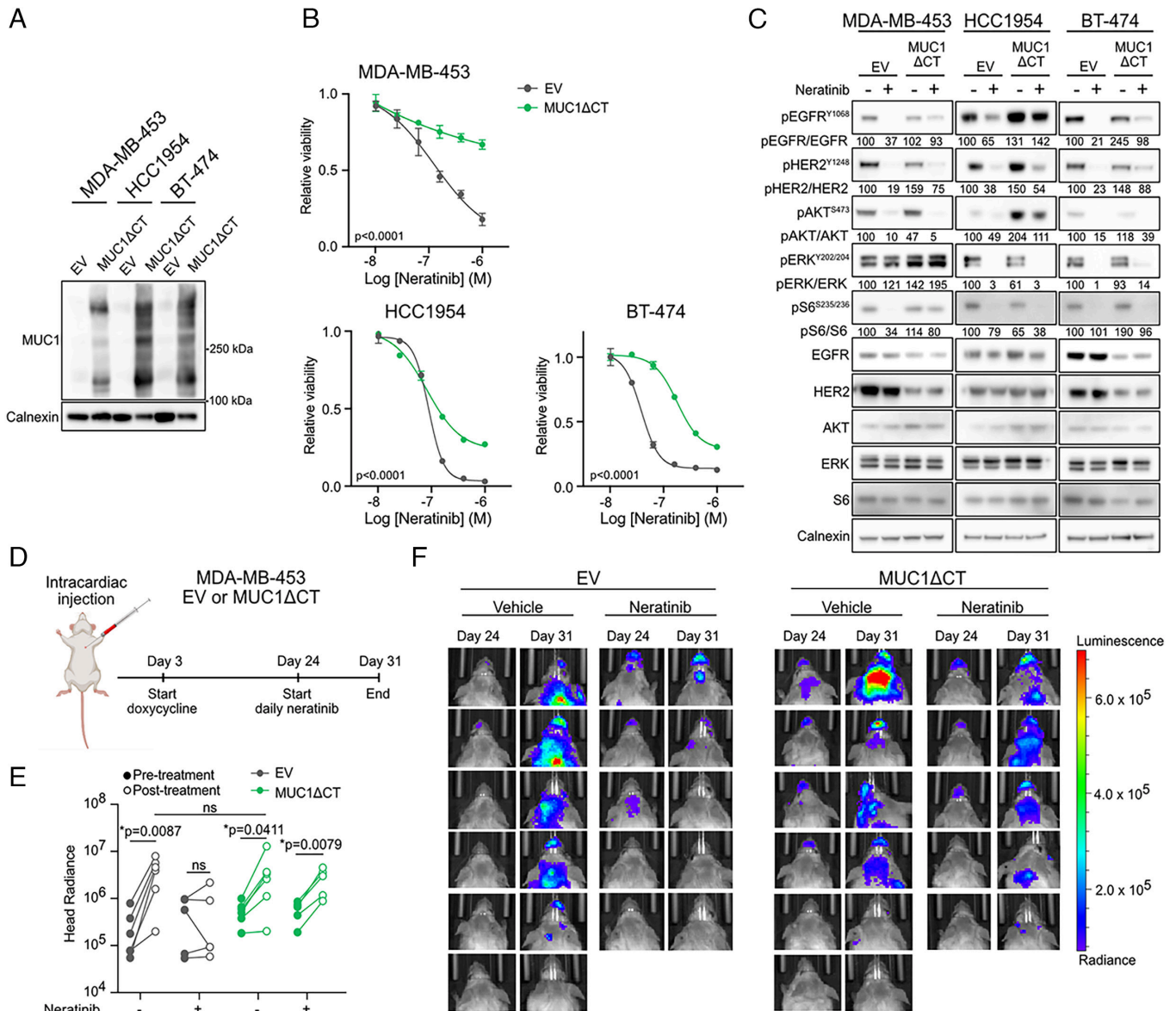

Fig. 4. An increased glycocalyx decreases neratinib sensitivity. (*A*) MUC1 immunoblot analysis of cells transduced with empty vector (EV) or MUC1ΔCT. Calnexin was used as loading control. (*B*) Relative cell viability of cancer cells expressing EV or MUC1ΔCT construct in the presence of increasing concentration of neratinib (two-way ANOVA, mean, and SEM). (*C*) Immunoblot analysis of EGFR/HER2 signaling pathway components in EV or MUC1ΔCT expressing cancer cells in the presence or absence of 50 nM neratinib. (*D*) Schematic of experimental brain metastasis induced by cardiac injection of MDA-MB-453 cells transduced with EV or MUC1ΔCT. Expression of MUC1ΔCT was induced by doxycycline in drinking water three days after cardiac injection. Mice were treated with daily gavage of 40 mg/kg of neratinib for 1 wk, starting 3 wk after cell injection. (*E*) Head radiance (photon/s/cm^2/sr) of mice at day 24 (pretreatment) and day 31 (posttreatment) treated with vehicle or neratinib (n = 5 to 6 mice per group, Mann–Whitney between pre- and posttreatment). (*F*) Bioluminescence images at day 24 (pretreatment) and day 31 (posttreatment).

to enhance cancer cell glycocalyx after initial dissemination and seeding. Brain metastases were allowed to develop for 3 wk after which 40 mg/kg of neratinib or vehicle was administered by oral gavage daily for one more week (Fig. 4D). The expression of MUC1ΔCT did not have an impact on overall brain metastasis burden, but the response to neratinib was muted compared to EV control cells (Fig. 4 E and F and SI Appendix, Fig. S6C). Indeed, neratinib treatment reduced the growth of brain metastases derived from EV-expressing cancer cells, but had no significant effect on brain metastases formed by MUC1ΔCT-expressing cells (Fig. 4 E and F). These results suggest that increased glycocalyx is a mechanism of neratinib resistance in HER2+ breast cancer brain metastases, and blocking glycoproteins could improve the efficacy of HER2-targeting therapies.

Discussion

The tumor microenvironment is a key regulator of tumor progression, metastasis, and therapy resistance. We and others have shown that cancer-associated fibroblasts in primary tumors promote resistance to neoadjuvant treatment (23, 37). However, cancer-associated mortality is largely due to metastatic disease and our understanding of the metastatic TME is relatively limited compared to that of primary tumors. Brain metastasis of breast cancer is one of the deadliest forms of the disease with the shortest disease-specific survival (1, 2) that is especially common in patients with HER2-positive and triple-negative breast cancer (3). While the recent development of various HER2-targeting therapeutic agents including small molecule inhibitors (e.g., neratinib and tucatinib) and antibody-drug conjugates (e.g., trastuzumab deruxtecan—T-DXd) has been improving treatment outcomes, effective therapies for metastatic disease are limited and therapeutic resistance is especially a major clinical challenge in brain metastases (38). Treatment resistance of brain metastases is in part due to the unique brain microenvironment including relative immune exclusion and special ECM and stromal cell populations. Thus, gaining a deeper understanding of breast cancer and brain stromal cell interactions is key for the design of more effective therapeutic strategies for these patients. Here, we used a Synthetic Notch-based reporter system (25, 39) to unravel a mechanism by which direct contact of HER2+ breast cancer cells with BMSCs increases resistance to neratinib. Specifically, we found that direct BMSC contact induces a shift in cancer cell transcriptomic and epigenetic profiles and up-regulates the expression of several mucins.

The BMSC primary cultures we derived from breast cancer brain metastases and used in this study were mainly composed of pericytes and vascular smooth-muscle cells collectively called mural cells. Endothelial cells and mural cells form the blood–tumor barrier in brain metastases, and they interact closely with cancer cells (40). Prior studies investigating the effect of endothelial and mural cells on brain metastasis development revealed their important roles in immune regulation (13). In our study, we found that their direct interaction with breast cancer cells also induces resistance to HER2-targeting agents.

Our RNA-seq profiling of BMSC contact and no-contact cancer cells revealed that genes associated with EMT, apical junctions, hypoxia, and apoptosis were up-regulated in both HER2+ cell lines when they are in contact with BMSCs. EMT and hypoxia have been associated with treatment resistance in a wide array of cancer types and therapeutic agents (24). Thus, the upregulation of these pathways by BMSC contact is likely contributing to neratinib resistance. Although, we have not delineated the details of how BMSC contact triggers this phenotypic switch in cancer cells, RNA-seq and ATAC-seq predicted NR3C1, ESR1, FOXA1, and AR as upstream regulators of BMSC-induced transcriptional changes. FOXA1 and AR have been shown to induce genes

mediating resistance to HER2-targeted therapy including HER3 (41, 42), which is in line with our observations that cells in coculture display lower pHER2/HER2 levels implying decreased dependency on HER2. Transcription factors can have hundreds of downstream targets. Therefore, it is likely that BMSC coculture induces a multitude of changes in cancer cells via different signaling pathways and not all of these may be related to the increased glycocalyx that we followed up in more detail.

Both hypoxia (43) and EMT are also known to up-regulate protein glycosylation (15) suggesting that their activation by BMSC contact may contribute to the increased glycocalyx we observed in BMSC cocultures together with the transcriptional upregulation of MUC2 and MUC5B. Mucins can cause therapeutic resistance by creating a physical barrier inhibiting biomolecular interactions. For example, expression of MUC4 in HER2+ breast cancer cells masks HER2 extracellular domain reducing trastuzumab binding leading to treatment resistance (21). A global decrease of protein glycosylation was shown to increase trastuzumab binding, increase sensitivity to doxorubicin, and decrease sensitivity to growth factors including IGF-1 and EGF (22), highlighting the importance of protein glycosylation in treatment responses. Increased cell surface protein glycosylation creates steric hindrance (16) that can impact receptor tyrosine kinase signaling by affecting their membrane localization and internalization dynamic. Our data showed that an increase in bulky glycocalyx can reduce the total levels of EGFR and HER2 without affecting their phosphorylation. Bulky glycocalyx also establishes a kinetic funnel of active integrins (16). This integrin clustering activates FAK leading to downstream AKT activation, in cooperation with EGFR, resulting in increased proliferation and metastasis (17). In line with this, apical junctions were one of the top up-regulated pathways by BMSC contact including increased expression of ITGB4, CDH3, and MSN.

Our results demonstrating that treatment with the mucinase StcE was able to reverse BMSC contact–induced neratinib resistance, both in cell culture and in brain metastases of mice, clearly establish a role for mucins in brain metastasis stroma-induced therapeutic resistance. Thus, we propose that hindering the glycocalyx can be an effective approach to treat brain metastases, especially in HER2-positive breast cancer in combination with HER2-targeting agents.

Materials and Methods

Cell Lines and Tissue Culture. Breast cancer brain metastases were dissociated to single cells by collagenase and hyaluronidase digest as previously described (23, 44) and cultured in 50/50 mixture of DMEM-F12 10% FBS and MEGM with supplements for three to 10 passages prior to using them for coculture experiments. Coculture experiments were performed using the media specific for the cancer cells. Breast cancer cell lines were purchased from ATCC or provided by Arthur Pardee, Dana-Farber Cancer Institute (21NT cells). Cells were cultured in conditions recommended by the supplier and routinely tested for mycoplasma and murine pathogens.

SynNotch Reporter. Cancer cells were transduced with both pHR_Gal4UAS_tBFP_PGK_mCherry (Addgene plasmid # 79130; http://n2t.net/addgene:79130; RRID:Addgene_79130) (25) and pHR_PGK_LaG16_2_synNotch_Gal4VP64 (Addgene plasmid # 85421; http://n2t.net/addgene:85421; RRID:Addgene_85421) (39), which were a gift from Wendell Lim. Cells were collected and stained for 1 h at room temperature with a 1:50 dilution of Myc-tag (9B11)-647 (Cell Signaling Technology, #2233S). Cells were then sorted for 647+ (Myc-tag-positive), mCherry+, and BFP- populations to create stable SynNotch+ cell lines.

pHR_EGFPligand [Addgene plasmid # 79129 (25); http://n2t.net/addgene:79129; RRID:Addgene_79129] was a gift from Wendell Lim. This plasmid was modified using the Gateway cloning method to include a puromycin selection marker. First, using the pENTR D-TOPO (K2400-20) kit and the primers pHR DTOPO Fwd (caccggagcaaggcaggtggac) and pHR DTOPO Rev (gtcgcgggcctcagtcag), EGFPligand was cloned into pENTR. pLenti CMV Puro DEST (w118-1) was a gift from Eric Campeau & Paul Kaufman (Addgene plasmid # 17452; http://n2t.net/addgene:17452; RRID:Addgene_17452) and LR clonase II enzyme mix (ThermoFisher, #11791020) was then used to clone EGFPligand into pLenti_CMV_EGFPligand_PGK_puro final vector. BMSC3s were then transduced with pLenti_CMV_EGFPligand_PGK_puro and selected with 2 μg/mL puromycin. GFP+ cells were then sorted to create GFP+BMSC3 cell line.

MUC1ΔCT Overexpression Model. Cells were transduced with the lentiviral pLV-neo-rtTA tet-on system. After selection with G418 (350 to 800 μg/mL), cells were cotransfected (Lipofectamine 3000, Thermo Fisher, per the manufacturer's recommendation) with PiggyBac-MUC1ΔCT or PiggyBac-EV and PiggyBac transposase and selected with puromycin (1 to 3 μg/mL) as described in ref. 17. For functional assays, cells were treated with 1 μg/mL doxycycline (Sigma-Aldrich).

Cell Viability Assays. For dose curve analyses, 5,000 cancer cells were embedded in 5% Growth Factor Reduced Matrigel Matrix (Corning) in low-adhesion 96-well plates. For coculture, 500 brain stromal cells (10%) were added. Indicated treatments were added 1 d after seeding of the cells and cells were lysed 6 to 8 d after using cell lysis buffer (Promega). Addition of D-Luciferin (Perkin Elmer, 125 μg/mL) allowed the measurement of cancer cell viability by luminescence using Biotek Synergy plate reader. All compounds were purchased from Selleck Chemicals. For the mucinase viability assay, StcE (10 nM) (34) was added to the culture at the same time as neratinib.

RNA-seq Preparation and Analyses. For monoculture, one six-well low attachment plate per treatment was seeded with SynNotch+ cancer cells (MDA-MB-453 at 300,000 cells/well and HCC1954 at 150,000 cells/well) in a 5% Growth Factor Reduced Matrigel mix. For coculture samples, three six-well plates were seeded per treatment condition with SynNotch+ cancer cells and GFP+ BMSCs (MDA-MB-453 at 300,000 cells/well with GFP+BMSCs at 30,000 cells/well and HCC1954 at 150,000 cells/well with GFP+BMSCs at 50,000 cells/well). Organoids were allowed to form for 24 h, and then were treated with either DMSO or neratinib (500 nM for MDA-MB-453s and 75 nM for HCC1954s) for 48 h. Cells were then collected and dissociated into single-cell suspensions using 0.25% trypsin and sorted into GFP-mCherry+BFP+ or GFP-mCherry+BFP+ populations. RNA was isolated using the RNeasy Mini kit (Qiagen) following the manufacturer's instructions. The total RNA was measured by Agilent 2100 Bioanalyzer. RNA-seq libraries were prepared using the Clontech Low Input mRNA Library (Clontech SMARTer) v4 kit from less than 10 ng of purified total RNA according to the manufacturer's protocol. The concentrations of dsDNA libraries were measured by Qubit fluorometer and RT-qPCR, and sizes were measured by TapeStation 2200 (Agilent), to adjust molar quantity. RNA-seq data were processed using VIPER pipeline (45). Fastq files were aligned to the human reference GRCh37/hg19 genome using the STAR RNA-Seq aligner (version STAR_2.5.1b) (46) followed by transcript assembly using cufflinks v2.2.1 [9] and RseQC v2.6.2 (47). Differential gene expression analyses were performed on absolute gene counts for RNA-Seq data and raw read counts for transcriptomic profiling data using DESeq2 v1.18.1 (48). GSEA was performed using the Broad GSEA Application (GSEA Java; v4.1.0) with Hallmark gene sets v7.4 (26, 27). The complete list of genes preranked by −log10(Padj) adjusted for the sign of log2-fold change (log2FC) of the prior differential gene expression analysis was used. We used the q value <0.25 recommended by broad GSEA software. The glycosylation gene signatures were taken from GSEA and (16, 49) to calculate enrichment scores using GSVA package (50).

ATAC-seq Preparation and Analyses. For monoculture, two 6-well low attachment plates per treatment were seeded with mCherry+ cancer cells (MDA-MB-453 at 200,000 cells/well and HCC1954 at 150,000 cells/well) in a 5% Growth Factor Reduced Matrigel mix. For coculture samples, two 6-well plates were seeded per treatment condition with SynNotch+ cancer cells and GFP+ BMSCs (MDA-MB-453 at 200,000 cells/well with GFP+BMSCs at 400,000 cells/well and HCC1954 at 150,000 cells/well with GFP+BMSCs at 300,000 cells/well). Organoids were allowed to form for 24 h, and then were treated with either DMSO or Neratinib (500 nM for MDA-MB-453s and 50 nM for HCC1954s) for 7 d. Cells were then collected and dissociated into single-cell suspensions using 0.25% trypsin and sorted into GFP-mCherry+ populations. 300,000 cells were viably frozen in 1 mL freezing media and transposed DNA fragments were obtained using OMNI-ATAC protocol. PCR amplification and purification were conducted and the Qiagen cleanup kit was applied to obtain purified DNA of at least 10 ng per sample.

Peak calling and data analysis. All samples were processed through the computational pipeline developed by the Dana-Farber Cancer Institute Center for Functional Cancer Epigenetics using primarily open-source programs (51, 52). Sequence tags were aligned with Burrows-Wheeler Aligner (BWA) (53) to build hg19 and uniquely mapped, nonredundant reads were retained. These reads were used to generate binding sites with Model-Based Analysis of ChIP-Seq 2 (MACS v2.1.1.20160309), with a q-value false discovery rate (FDR) threshold of 0.01 (54). We evaluated multiple quality control criteria based on alignment information and peak quality: i) sequence quality score; ii) uniquely mappable reads (reads that can only map to one location in the genome); iii) uniquely mappable locations (locations that can only be mapped by at least one read); iv) peak overlap with Velcro regions, a comprehensive set of locations–also called consensus signal artifact regions–in the genome that have anomalous, unstructured high signal or read counts in next-generation sequencing experiments independent of cell line and of type of experiment; v) number of total peaks (the minimum required was 5,000); vi) high-confidence peaks (the number of peaks that are tenfold enriched over background); vii) percentage overlap with known DHS sites derived from the ENCODE Project (the minimum required to meet the threshold was 80%); and viii) peak conservation (a measure of sequence similarity across species based on the hypothesis that conserved sequences are more likely to be functional).

Differential binding analyses. Peaks from all samples were merged to create a union set of sites for each genomic region using bedops (55). Sample-sample correlation and differential peaks analysis were performed by the CoBRA pipeline (51). Read densities were calculated for each peak for each sample and used for the comparison of cistromes across samples. Sample similarity was determined by hierarchical clustering using the Spearman correlation between samples. Differential peaks were identified by DEseq2 with adjusted *P*-value ≤0.05. A total number of reads in each sample was applied to the size factor in DEseq2, which can normalize the sequencing depth between samples.

Genomic feature distributions were annotated using peak files from significantly changed regions in each depicted condition. CHIPseeker (v. 1.28.3) (56) was used for annotation to hg19Patch10. Pathway enrichment analysis for significantly gained peaks in DMSO coculture vs monoculture conditions was calculated using ChIP-Enrich (v.0.1.0) (57) in "Hybrid-Enrich" mode using peaks close to nearest genes. "Reactome" database was used for pathway annotation to hg19 genome.

Glycosylation Signature Analysis in Brain Metastatic Samples. RNA-seq profiling from 22 pairs of intrapatient matched primary and brain metastatic tumors were obtained from Vareŝlija et al. (32). Briefly, raw counts were downloaded from the resource paper, which were then converted to Log2 transformed TMM-normalized counts per million [log2 (TMM-CPM + 1)] using edgeR (58). ECM glycoprotein signatures were downloaded from mSigDB with the accession number M3008. To eliminate the influence from normal brain and breast background differences, we first calculated differentially expressing genes (FDR < 0.05) between normal brain to breast using the GTEX (59) dataset and filtered out those differential genes from the targeted signature. The enrichment scores for the filtered signature were calculated using GSVA (50). The Wilcoxon paired sample signed rank test was used to examine the difference between the paired primary tumor and brain metastasis.

Immunofluorescence Staining. For organoid staining, cells were plated in 5% Growth Factor Reduced Matrigel Matrix (Corning) and 3 to 5 d later were harvested in cold PBS. Organoids were then washed with 1X Carbo-Free Blocking Solution (Vector Laboratories) for 5 min and stained using biotin-StcE^E447D (34) in PBS for 1 h on ice. After a wash with PBS, cells were stained with Streptavidin-647 (Life Technologies, 1:1,000) for 20 min at room temperature and washed again with PBS. Cells were then resuspended in a drop of Vectashield (Vector Laboratories) to mount on glass slides and image right away using the Nikon ECLIPSE Ti2-E

fluorescence microscope. Quantifications were done using imageJ where MFI was calculated for manually surrounded organoids. For BMSC staining, cells were plated on collagen-coated glass slides, fixed with 4% PFA, permeabilized with 0.1% Triton-X 100 in PBS and blocked with 1% BSA-PBS before incubation with primary antibodies [anti-PDGFRβ (BioRad 7460-3104, 1:200) and anti-αSMA (Fisher, MS113P, 1:500)] overnight. After washes with PBS, slides were incubated with secondary antibody for 30 min (Life Technologies, Alexa Fluor 647 anti-Mouse IgG2a, Alexa Fluor 488 anti-Mouse IgG1, 1:500) and imaged as described.

Immunoblot Analyses. Cells were plated in 5% Growth Factor Reduced Matrigel Matrix (Corning) and 3 to 5 d later were treated with 10 nM StcE for 1 h followed by 50 nM neratinib (Selleck Chemicals) for 1 h. Cells were then collected and washed in cold PBS. Cells were lysed with 100 μL RIPA lysis buffer (50 mM Tris pH 7.6, 0.1% SDS, 1% NP-40, 150 mM NaCl, 5 nM EDTA) containing phosphatase and protease inhibitors. Protein concentration was quantified using Pierce™ 660 nm Protein Assay Reagent (Thermo Fisher) protein assay and proteins were heat-denatured in the presence of β-mercapto-ethanol. Equal quantities of protein were loaded onto a NuPAGE Novex 4 to 12% gradient Bis-Tris gel (Fisher Scientific) and separated by electrophoresis. Proteins were transferred onto PVDF membranes (BioRad) using a wet NuPAGE Transfer buffer system with transfer buffer containing 20% methanol for 1 h 30 at 90 V. The membranes were then blocked using 5% milk in 0.1% Tween20 TBS (TBST) for 1 h at room temperature followed by an overnight incubation with primary antibodies at 1:1,000 in antibody diluent (LI-COR) [pEGFR Y1068 (CST 2234), EGFR (CST 3777S), pHER2 Y1248 (CST 2247S), HER2 (Abcam ab16901), pAKT S473 (CST 9271S), AKT (CST 9272S), pERK Tyr202/204 (CST 9101S), ERK½ (CST 9102S), pS6 S235/236 (CST 2211s), S6 Ribosomal Protein (5G10) (CST 2217), Calnexin (CST 2679S), and MUC1 (555925, BD)]. Membranes were washed and incubated for 30 min at room temperature with appropriate secondary antibodies [anti-mouse HRP (Life Technologies, 62-6520, 1:5,000) or anti-rabbit HRP (Life Technologies, 65-6120, 1:5,000)], then washed and developed with Clarity™ Western ECL substrate (Bio-Rad), and imaged using ChemiDoc MP imaging system (Bio-Rad).

Animal Experiments. Animal experiments were performed following protocol #11-023 approved by the DFCI Institutional Animal Care and Use Committee adhering to NIH guidelines. Experimental metastasis assay by intracardiac injection was performed using 6-wk-old female NOD.Cg-Prkdcscid Il2rgtm1Wjl/SzJ (NSG) mice obtained from the Jackson Laboratory. Mice were anesthetized using constant isoflurane inhalation and 250,000 cells in 100 μL of PBS were injected directly in the left ventricle. Successful injections were validated by bioluminescence imaging 24 h later using Xenogen imager. 625 PPM Doxycycline Diet (Mod LabDiet) was given to the mice 3 d after injection. Three weeks following injection, mice were treated with 40 mg/kg of neratinib in 0.5% methylcellulose or vehicle by oral gavage of 200 μL daily. Bioluminescence images were taken before and after the week of treatment to compare progression. Brains were embedded in paraffin, sectioned, and stained with hematoxylin and eosin (H&E) to confirm the brain metastasis observed with bioluminescence.

Statistical Analyses. The normal distribution of data was initially assessed using the Shapiro–Wilk test. If the data for matched comparisons did not meet the normal distribution criteria, nonparametric tests were employed. In the case of single comparisons with normal distribution, Student's t-test was performed. For the nonpaired single comparisons, Mann–Whitney or Wilcoxon tests were utilized. For multiple comparisons, a one-way ANOVA corrected for multiple comparisons was applied. All statistical analyses were conducted with a 95% CI, and corresponding significant P-values ($P > 0.05$) were provided for each experiment.

Data, Materials, and Software Availability. Raw and processed RNA-seq and ATAC-seq data were deposited to NCBI GEO database under accession number GSE249574 (60).

Author affiliations: ªDepartment of Medical Oncology, Dana-Farber Cancer Institute, Boston, MA 02215; ᵇDepartment of Medicine, Harvard Medical School, Boston, MA 02115; ᶜDepartment of Medicine, Brigham and Women's Hospital, Boston, MA 02115; ᵈCenter for Functional Cancer Epigenetics, Dana-Farber Cancer Institute, Boston, MA 02215; ᵉDepartment of Chemistry, Stanford University, Stanford, CA 94305; ᶠCenter for Bioengineering and Tissue Regeneration, University of California San Francisco, San Francisco, CA 94143; ᵍHHMI, Stanford University, Stanford, CA 94305; ʰSarafan ChEM-H, Stanford University, Stanford, CA 94305; ⁱHelen Diller Comprehensive Cancer Center, University of California San Francisco, San Francisco, CA 94143; ʲDepartment of Surgery, University of California San Francisco, San Francisco, CA 94143; ᵏDepartment of Bioengineering and Therapeutic Sciences, University of California San Francisco, San Francisco, CA 94143; ˡDepartment of Radiation Oncology, University of California San Francisco, San Francisco, CA 94143; and ᵐEli and Edythe Broad Center of Regeneration Medicine and Stem Cell Research, University of California San Francisco, San Francisco, CA 94143

1. H. Dillekås, M. S. Rogers, O. Straume, Are 90% of deaths from cancer caused by metastases? *Cancer Med.* **8**, 5574–5576 (2019).
2. P. W. Sperduto *et al.*, Survival in patients with brain metastases: Summary report on the updated diagnosis-specific graded prognostic assessment and definition of the eligibility quotient. *J. Clin. Oncol.* **38**, 3773–3784 (2020).
3. Y. Gong, Y. R. Liu, P. Ji, X. Hu, Z. M. Shao, Impact of molecular subtypes on metastatic breast cancer patients: A SEER population-based study. *Sci. Rep.* **7**, 45411 (2017).
4. M. Kuksis *et al.*, The incidence of brain metastases among patients with metastatic breast cancer: A systematic review and meta-analysis. *Neuro Oncol.* **23**, 894–904 (2021).
5. D. Trapani, A. A. Aizer, N. U. Lin, Multidisciplinary management of brain metastasis from breast cancer. *Hematol. Oncol. Clin. North Am.* **37**, 183–202 (2023).
6. O. Tonyali *et al.*, Risk factors for brain metastasis as a first site of disease recurrence in patients with HER2 positive early stage breast cancer treated with adjuvant trastuzumab. *Breast* **25**, 22–26 (2016).
7. S. Kabraji *et al.*, Drug resistance in HER2-positive breast cancer brain metastases: Blame the barrier or the brain? *Clin. Cancer Res* **24**, 1795–1804 (2018).
8. K. E. de Visser, J. A. Joyce, The evolving tumor microenvironment: From cancer initiation to metastatic outgrowth. *Cancer Cell* **41**, 374–403 (2023).
9. S. Qiao, Y. Qian, G. Xu, C. Luo, Z. Zhang, Long-term characterization of activated microglia/macrophages facilitating the development of experimental brain metastasis through intravital microscopic imaging. *J. Neuroinflammation* **16**, 4 (2019).
10. Q. Zeng *et al.*, Synaptic proximity enables NMDAR signalling to promote brain metastasis. *Nature* **573**, 526–531 (2019).
11. Q. Chen *et al.*, Carcinoma-astrocyte gap junctions promote brain metastasis by cGAMP transfer. *Nature* **533**, 493–498 (2016).
12. D. F. Quail, J. A. Joyce, The microenvironmental landscape of brain tumors. *Cancer Cell* **31**, 326–341 (2017).
13. L. Bejarano *et al.*, Interrogation of endothelial and mural cells in brain metastasis reveals key immune-regulatory mechanisms. *Cancer Cell* **42**, 378–395.e10 (2024), 10.1016/j.ccell.2023.12.018.
14. M. Valiente *et al.*, Serpins promote cancer cell survival and vascular co-option in brain metastasis. *Cell* **156**, 1002–1016 (2014).
15. A. Buffone, V. M. Weaver, Don't sugarcoat it: How glycocalyx composition influences cancer progression. *J. Cell Biol.* **219**, e201910070 (2020).
16. M. J. Paszek *et al.*, The cancer glycocalyx mechanically primes integrin-mediated growth and survival. *Nature* **511**, 319–325 (2014).
17. E. C. Woods *et al.*, A bulky glycocalyx fosters metastasis formation by promoting G1 cell cycle progression. *Elife* **6**, e25752 (2017).
18. K. J. Metcalf *et al.*, Immunosuppressive glycoproteins associate with breast tumor fibrosis and aggression. *Matrix Biol. Plus* **14**, 100105 (2022).
19. D. W. Kufe, Mucins in cancer: Function, prognosis and therapy. *Nat. Rev. Cancer* **9**, 874–885 (2009).
20. M. A. Hollingsworth, B. J. Swanson, Mucins in cancer: Protection and control of the cell surface. *Nat. Rev. Cancer* **4**, 45–60 (2004).
21. P. Nagy *et al.*, Decreased accessibility and lack of activation of ErbB2 in JIMT-1, a herceptin-resistant, MUC4-expressing breast cancer cell line. *Cancer Res.* **65**, 473–482 (2005).
22. D. Peiris *et al.*, Cellular glycosylation affects Herceptin binding and sensitivity of breast cancer cells to doxorubicin and growth factors. *Sci. Rep.* **7**, 43006 (2017).
23. A. Marusyk *et al.*, Spatial proximity to fibroblasts impacts molecular features and therapeutic sensitivity of breast cancer cells influencing clinical outcomes. *Cancer Res.* **76**, 6495–6506 (2016).
24. A. Marusyk, M. Janiszewska, K. Polyak, Intratumor heterogeneity: The Rosetta Stone of therapy resistance. *Cancer Cell* **37**, 471–484 (2020).
25. L. Morsut *et al.*, Engineering customized cell sensing and response behaviors using synthetic notch receptors. *Cell* **164**, 780–791 (2016).
26. A. Subramanian *et al.*, Gene set enrichment analysis: A knowledge-based approach for interpreting genome-wide expression profiles. *Proc. Natl. Acad. Sci. U.S.A.* **102**, 15545–15550 (2005).
27. A. Liberzon *et al.*, The Molecular Signatures Database (MSigDB) hallmark gene set collection. *Cell Syst.* **1**, 417–425 (2015).
28. Q. Qin *et al.*, Lisa: Inferring transcriptional regulators through integrative modeling of public chromatin accessibility and ChIP-seq data. *Genome Biol.* **21**, 32 (2020).
29. M. Hu *et al.*, Distinct epigenetic changes in the stromal cells of breast cancers. *Nat. Genet* **37**, 899–905 (2005).
30. J. Albrengues *et al.*, Epigenetic switch drives the conversion of fibroblasts into proinvasive cancer-associated fibroblasts. *Nat. Commun.* **6**, 10204 (2015).

31. Q. Yang *et al.*, m6A regulator-mediated methylation modification patterns and tumor microenvironment cell-infiltration characterization in head and neck cancer. *Front Cell Dev. Biol* **9**, 803141 (2021).

32. D. Varešlija *et al.*, Transcriptome characterization of matched primary breast and brain metastatic tumors to detect novel actionable targets. *J. Natl. Cancer Inst.* **111**, 388–398 (2019).

33. C. R. Shurer *et al.*, Genetically encoded toolbox for glycocalyx engineering: Tunable control of cell adhesion, survival, and cancer cell behaviors. *ACS Biomater. Sci. Eng* **4**, 388–399 (2018).

34. D. J. Shon *et al.*, An enzymatic toolkit for selective proteolysis, detection, and visualization of mucin-domain glycoproteins. *Proc. Natl. Acad. Sci. U.S.A.* **117**, 21299–21307 (2020).

35. K. Pedram *et al.*, Design of a mucin-selective protease for targeted degradation of cancer-associated mucins. *Nat. Biotechnol.* **4**, 388–399 (2023), 10.1038/s41587-023-01840-6.

36. S. A. Malaker *et al.*, The mucin-selective protease StcE enables molecular and functional analysis of human cancer-associated mucins. *Proc. Natl. Acad. Sci. U.S.A.* **116**, 7278–7287 (2019).

37. R. Kalluri, The biology and function of fibroblasts in cancer. *Nat. Rev. Cancer* **16**, 582–598 (2016).

38. A. S. Achrol *et al.*, Brain metastases. *Nat. Rev. Dis. Primers* **5**, 5 (2019).

39. K. T. Roybal *et al.*, Engineering T cells with customized therapeutic response programs using synthetic notch receptors. *Cell* **167**, 419–432.e6 (2016).

40. K. G. Blecharz, R. Colla, V. Rohde, P. Vajkoczy, Control of the blood–brain barrier function in cancer cell metastasis. *Biol. Cell* **107**, 342–371 (2015).

41. M. Ni *et al.*, Targeting androgen receptor in estrogen receptor-negative breast cancer. *Cancer Cell* **20**, 119–131 (2011).

42. S. P. Angus *et al.*, FOXA1 and adaptive response determinants to HER2 targeted therapy in TBCRC 036. *NPJ Breast Cancer* **7**, 51 (2021).

43. M. I. Khan, S. Rath, V. M. Adhami, H. Mukhtar, Hypoxia driven glycation: Mechanisms and therapeutic opportunities. *Semin. Cancer Biol.* **49**, 75–82 (2018).

44. M. Allinen *et al.*, Molecular characterization of the tumor microenvironment in breast cancer. *Cancer Cell* **6**, 17–32 (2004).

45. M. Cornwell *et al.*, VIPER: Visualization Pipeline for RNA-seq, a Snakemake workflow for efficient and complete RNA-seq analysis. *BMC Bioinformatics* **19**, 135 (2018).

46. A. Dobin *et al.*, STAR: Ultrafast universal RNA-seq aligner. *Bioinformatics* **29**, 15–21 (2013).

47. L. Wang, S. Wang, W. Li, RSeQC: Quality control of RNA-seq experiments. *Bioinformatics* **28**, 2184–2185 (2012).

48. M. I. Love, W. Huber, S. Anders, Moderated estimation of fold change and dispersion for RNA-seq data with DESeq2. *Genome Biol.* **15**, 550 (2014).

49. J. M. Barnes *et al.*, A tension-mediated glycocalyx-integrin feedback loop promotes mesenchymal-like glioblastoma. *Nat. Cell Biol.* **20**, 1203–1214 (2018).

50. S. Hänzelmann, R. Castelo, J. Guinney, GSVA: Gene set variation analysis for microarray and RNA-Seq data. *BMC Bioinformatics* **14**, 7 (2013).

51. X. Qiu *et al.*, CoBRA: Containerized bioinformatics workflow for reproducible ChIP/ATAC-seq analysis. *Genom. Proteom. Bioinform.* **19**, 652–661 (2021).

52. L. Taing *et al.*, CHIPS: A Snakemake pipeline for quality control and reproducible processing of chromatin profiling data [version 1; peer review: 2 approved with reservations, 2 not approved]. *F1000Research* **10**, 517 (2021).

53. H. Li, R. Durbin, Fast and accurate short read alignment with Burrows-Wheeler transform. *Bioinformatics* **25**, 1754–1760 (2009).

54. Y. Zhang *et al.*, Model-based analysis of ChIP-Seq (MACS). *Genome Biol.* **9**, R137 (2008).

55. S. Neph *et al.*, BEDOPS: High-performance genomic feature operations. *Bioinformatics* **28**, 1919–1920 (2012).

56. G. Yu, L.-G. Wang, Q.-Y. He, ChIPseeker: An R/Bioconductor package for ChIP peak annotation, comparison and visualization. *Bioinformatics* **31**, 2382–2383 (2015).

57. R. P. Welch *et al.*, ChIP-Enrich: Gene set enrichment testing for ChIP-seq data. *Nucleic Acids Res.* **42**, e105 (2014).

58. M. D. Robinson, D. J. McCarthy, G. K. Smyth, edgeR: A Bioconductor package for differential expression analysis of digital gene expression data. *Bioinformatics* **26**, 139–140 (2010).

59. J. Lonsdale *et al.*, The Genotype-Tissue Expression (GTEx) project. *Nat. Genet.* **45**, 580–585 (2013).

60. M.-A. Goyette *et al.*, Cancer-stromal cell interactions in breast cancer brain metastases induce glycocalyx-mediated resistance to HER2-targeting therapies. NCBI GEO. https://www.ncbi.nlm.nih.gov/geo/query/acc.cgi?acc=GSE249574. Deposited 7 December 2023.